EBioMedicine 47 (2019) 98–113

Contents lists available at ScienceDirect

EBioMedicine

journal homepage: www.ebiomedicine.com

EBioMedicine
Published by THE LANCET

Research paper

Lymphatic vessel remodeling and invasion in pancreatic cancer progression

Chia-Ning Shen [a,b], King-Siang Goh [a], Chi-Ruei Huang [a], Tsai-Chen Chiang [c], Chih-Yuan Lee [c], Yung-Ming Jeng [d], Shih-Jung Peng [e,f], Hung-Jen Chien [e], Mei-Hsin Chung [e,g], Ya-Hsien Chou [e], Chi-Che Hsieh [a], Subhash Kulkarni [h], Pankaj J. Pasricha [h], Yu-Wen Tien [c,*], Shiue-Cheng Tang [e,f,**]

[a] Genomics Research Center, Academia Sinica, Taipei, Taiwan
[b] Institute of Biochemistry and Molecular Biology, National Yang-Ming University, Taipei, Taiwan
[c] Department of Surgery, National Taiwan University Hospital, Taipei, Taiwan
[d] Department of Pathology, National Taiwan University Hospital, Taipei, Taiwan
[e] Institute of Biotechnology, National Tsing Hua University, Hsinchu, Taiwan
[f] Department of Medical Science, National Tsing Hua University, Hsinchu, Taiwan
[g] Department of Pathology, National Taiwan University Hospital – Hsinchu Branch, Hsinchu, Taiwan
[h] Division of Gastroenterology and Hepatology, Johns Hopkins University School of Medicine, Baltimore, MD, USA

ARTICLE INFO

Article history:
Received 28 October 2018
Received in revised form 15 August 2019
Accepted 15 August 2019
Available online 5 September 2019

Keywords:
Cancer invasion
Metastasis
Kras^{G12D} mutation
Lymphangiogenesis
Lymphatic vessel
Lymphovascular invasion
Pancreatic cancer
Pancreatic intraepithelial neoplasia
Pancreatic ductal adenocarcinoma
p53 mutation

ABSTRACT

Background: The lymphatic system is involved in metastasis in pancreatic cancer progression. In cancer staging, lymphatic spread has been used to assess the invasiveness of tumor cells. However, from the endothelium's perspective, the analysis downplays the peri-lesional activities of lymphatic vessels. This unintended bias is largely due to the lack of 3-dimensional (3-D) tissue information to depict the lesion microstructure and vasculature in a global and integrated fashion.
Methods: We targeted the pancreas as the model organ to investigate lymphatic vessel remodeling in cancer lesion progression. Transparent pancreases were prepared by tissue clearing to facilitate deep-tissue, tile-scanning microscopy for 3-D lymphatic network imaging.
Findings: In human pancreatic ductal adenocarcinoma, we identify the close association between the pancreatic intraepithelial neoplasia (PanIN) lesions and the lymphatic network. In mouse models of PanIN (*elastase-Cre*ER;LSL-*Kras*^{G12D} and *elastase-Cre*ER;LSL-*Kras*^{G12D};*p53*$^{+/-}$), the 3-D image data reveal the peri-lesional lymphangiogenesis, endothelial invagination, formation of the bridge/valve-like luminal tubules, vasodilation, and luminal invasion. In the orthotopic mouse model of pancreatic cancer, we identify the localized, graft-induced lymphangiogenesis and the peri- and intra-tumoral lymphatic vessel invasion.
Interpretation: The integrated view of duct lesions and vascular remodeling suggests an active role, rather than a passive target, of lymphatic vessels in the metastasis of pancreatic cancer. Our 3-D image data provide insights into the pancreatic cancer microenvironment and establish the technical and morphological foundation for systematic detection and 3-D analysis of lymphatic vessel invasion.
Fund: Taiwan Academia Sinica (AS-107-TP-L15 and AS-105-TP-B15), Ministry of Science and Technology (MOST 106-2321-B-001-048, 106-0210-01-15-02, 106-2321-B-002-034, and 106-2314-B-007-004-MY2), and Taiwan National Health Research Institutes (NHRI EX107-10524EI).

1. Introduction

The lymphatic drainage of pancreas is achieved by an intricate network of lymphatic vessels and nodes to collect the interstitial fluids for water maintenance and immune surveillance [1,2]. When diseases such as pancreatitis or neoplasm occur, the lymphatic system plays an essential role in host defenses in response to inflammation and malignant transformation. Clinically, the association of lymphatics with pancreatic duct lesion progression is demonstrated by the lymph node

Abbreviations: 2-D, 2-dimensional; 3-D, 3-dimensional; EGFP, enhanced green fluorescence protein; EK mice, *elastase-Cre*ER;LSL-*Kras*^{G12D} mice; EKP mice, *elastase-Cre*ER;LSL-*Kras*^{G12D};*p53*$^{+/-}$ mice; H&E, hematoxylin and eosin; Lyve1, lymphatic vessel endothelial hyaluronan receptor 1; PanIN, pancreatic intraepithelial neoplasia; PDAC, pancreatic ductal adenocarcinoma.

* Correspondence to: Y.-W. Tien, Department of Surgery, National Taiwan University Hospital, Taipei, Taiwan.
** Correspondence to: S.-C. Tang, Institute of Biotechnology, National Tsing Hua University, Hsinchu, Taiwan.
E-mail addresses: ywtien5106@ntu.edu.tw (Y.-W. Tien), sctang@life.nthu.edu.tw (S.-C. Tang).

https://doi.org/10.1016/j.ebiom.2019.08.044

Research in context

Evidence before this study

Lymph node metastasis has been clinically used in pancreatic cancer staging. However, in pathology, characterization of the lymphatic association with the precancerous/cancerous lesions remains a challenging task due to the lack of imaging tools to visualize the lymphatic vessels in a 3-D space continuum with high definition.

Added value of this study

Taking full advantage of the recent breakthrough in 3-D histology with tissue clearing, in this study we prepare transparent pancreases to characterize the lymphatic vessel remodeling and invasion in cancer progression. Using the human pancreases, we present the map of lymphatic vasculature and the associated microstructural and lymphatic network remodeling in pancreatic ductal adenocarcinoma (PDAC). In mice, we use the PDAC model to illustrate the duct lesion-lymphatic network association at its early stage, which otherwise cannot be revealed in the clinical condition. Importantly, at the advanced stage of lesion formation, we identify the parallel events of peri-lesional lymphangiogenesis, endothelial invagination, formation of the luminal tubules, vasodilation, and luminal invasion. These results provide insights into the lesion microenvironment and establish the technical and morphological foundation for systematic detection and 3-D analysis of lymphatic vessel invasion.

Implications of all the available evidence

Our 3-D image data indicate a highly plastic and dynamic lymphatic system in the pancreas that responds to the formation of duct lesions with proliferation and remodeling. The lymphangiogenesis and remodeling suggest an active role – rather than a passive target – of lymphatic vessels in the metastasis of pancreatic cancer.

metastasis in pancreatic ductal adenocarcinoma (PDAC) [3–7]. In particular, lymphatic spread has been used as a key prognostic factor to assess the invasiveness of tumor cells [4–6]. However, from the endothelium's perspective, the active responses of lymphatic vessels to tissue remodeling, such as injury and inflammation induced by cancer progression, have not been thoroughly investigated due to the lack of 3-dimensional (3-D) image data to analyze the dispersed lymphatic network in space.

Pathophysiologically, pancreatic duct lesion progression is a process of epithelial transformation, ranging from the formation of low-grade pancreatic intraepithelial neoplasia (PanIN) lesions to metastatic adenocarcinoma [8]. This process is often associated with inflammation (pancreatitis) and oncogenic *Kras* mutation, causing potential acinar-to-ductal metaplasia and unregulated epithelial proliferation, which in turn remodels the pancreatic microenvironment [9–13]. Particularly, the epithelial overgrowth leads to acinar atrophy and excessive stromal deposition in the pancreas [14–16].

The major stromal components of pancreatic duct lesions are the stellate cells (or myofibroblast-like cells), nerves (including glial cells), and microvessels (blood vessels/pericytes and lymphatic vessels) [14–18]. In cancer progression, the stellate cells create a desmoplastic environment, which hosts and supports the malignant epithelium and the neurovascular tissues; the latter in turn becomes potential targets for tumor invasion, leading to metastasis. Immunohistochemical analysis of the pancreatic cancer microenvironment reveals an overexpression of the lymphangiogenic growth factor VEGF-C and -D [19]. The overexpression indicates a favorable condition for lymphangiogenesis and lymphatic spread, which have been observed in other gastrointestinal tumors, such as the gastric and colorectal carcinomas [20–23].

To examine the lymphatic network in pancreatic duct lesion progression, in this study we prepare transparent pancreases via tissue clearing [18,24,25] for 3-dimensional (3-D) lymphatic network imaging. Importantly, in both human and mouse pancreases we identify the close association between the PanIN lesions and lymphatic network. Using the transgenic models of PanIN, we demonstrate that the lesion-lymphatic vessel association occurs at the early stage of lesion formation, which is magnified in pancreatitis with marked lymphangiogenesis and endothelial remodeling. Using the syngeneic mouse model of orthotopic cancer cell injection, we identify the localized lymphangiogenesis with tumor-vessel association. In both the transgenic and orthotopic models, our 3-D image data reveal lymphatic vessel invasion with high definition. Qualitative and quantitative analyses of the different phases and aspects of lymphatic vessel remodeling and invasion are presented and discussed in this report.

2. Materials and methods

2.1. Human pancreatic specimens

Collection and use of human tissues were approved by the Institutional Review Board of National Taiwan University Hospital. Normal human pancreases were obtained from the cadaveric donors. Specimens from three donors with normal HbA_{1c}, amylase, and lipase levels were used to establish the pancreatic lymphatic network. Pancreatic specimens with PanIN lesions were obtained from pancreatectomy for treatment of PDAC. Immediately after the operation, the dissected specimens were perfused with 1000 ml of saline through the splenic artery, which was cannulated with a Fr. 21-peripheral venous catheter, to remove the residual blood. Afterward, the tissues were fixed in 4% formaldehyde for 2 days and then washed in saline for 4 days at 4 °C [25]. Specimens were later sectioned to 350 μm in thickness by vibratome and transferred to 0.1% paraformaldehyde for preservation at 4 °C. Specimens from three PDAC patients (sex/age (years)/staging: male/77/T1N0, male/52/T2N0, and male/67/T3N0) were used to identify the peri-lesional lymphatic network.

2.2. Genetically engineered and syngeneic mouse models of pancreatic cancer

Normal pancreases and pancreases with PanIN lesions were harvested from the 14-week-old wild-type C57BL/6 (B6) mice (control), *elastase-Cre*ER;LSL-*Kras*^{G12D} mice (or EK mice; *elastase-Cre*ER × LSL-*Kras*^{G12D} mice) [18], and *elastase-Cre*ER;LSL-*Kras*^{G12D};*p53*$^{+/-}$ mice (or EKP mice; EK × B6.129S2-*Trp53*^{tm1Tyj}/J mice, Jackson Laboratory; stock number: 002101; this mouse line develops liver metastasis at the advanced stage). To examine the early-stage duct lesion formation, the EK mice were injected with tamoxifen at age 6 weeks (Sigma, St. Louis, MO, USA; 2 mg/injection, three injections in 1 week to induce *Cre*-mediated recombination) and then allowed for duct lesion development for the next 7 weeks. To examine the advanced duct lesion formation, the EK and EKP mice were injected with tamoxifen at age 6 weeks and followed by 3-week cerulein treatment (starting at age 7 weeks; Sigma, 0.25 mg/kg body weight, six injections per week) and 4-week tissue regrowth to induce large-scale development of PanIN lesions. B6 mice with 3-week cerulein treatment and 4-week tissue regrowth were used as the control. Overall, six normal and cerulein-treated B6 mice, six EK mice with early-stage duct lesions, and seven EK and EKP mice with advanced lesion formation were used to generate the representative images.

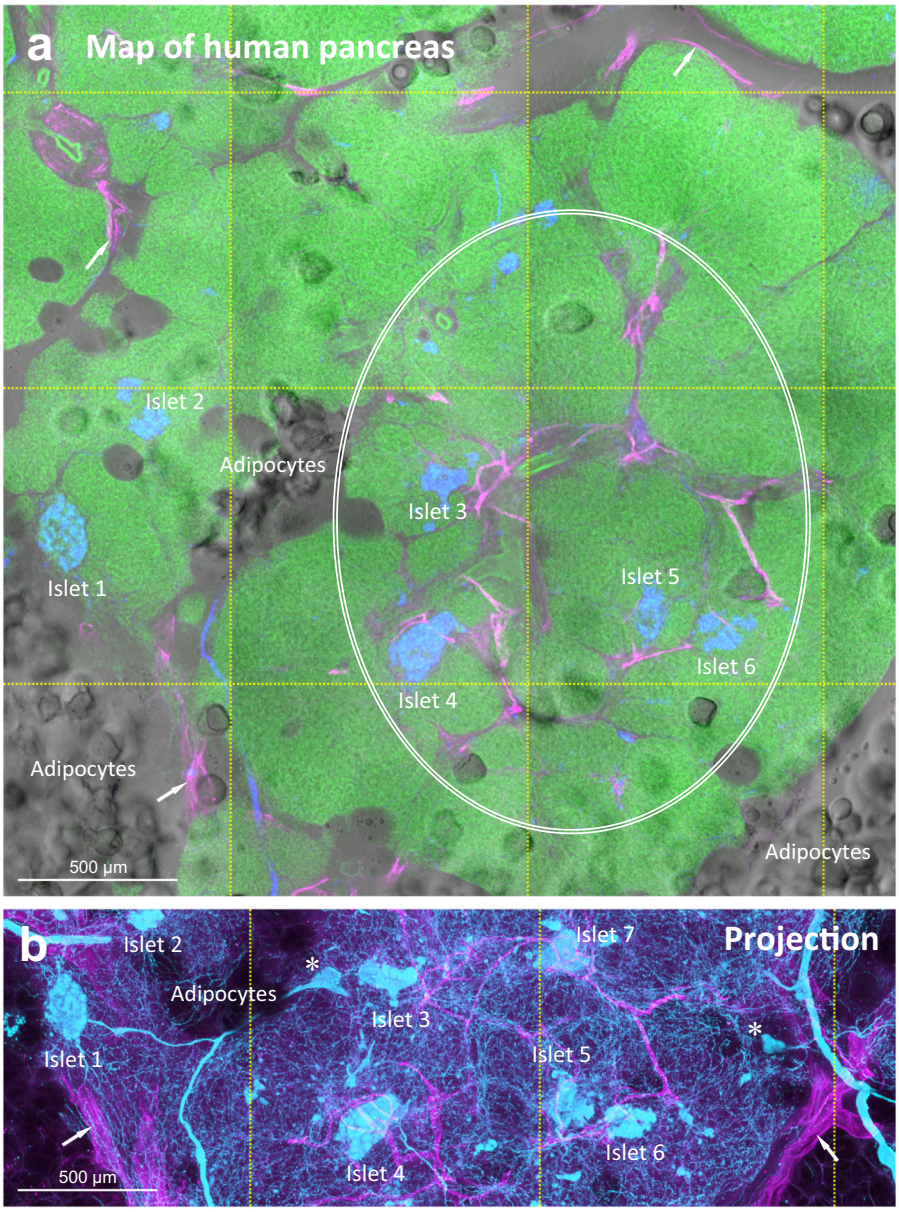

Fig. 1. Human pancreatic lymphatic network in health and around PanIN lesions. (a, b) 2-D tissue map and 3-D projection of pancreatic lymphatic network. Tile scanning and image stitching were used to generate the map. Lymphatic vessels (magenta, D2-40^{+}) reside at the peri-lobular space (arrows) and inside the parenchyma in association with the ducts and islets (oval, a). Neuroendocrine marker PGP9.5 staining (blue/cyan) reveals the neurolymphatic association and the endocrine islets. Islets are used as the landmarks (labeled with numbers) to correlate the pancreatic microstructure and lymphatic network in a and b (b focuses at the center of a, projection depth: 350 μm). Asterisks in b denote the intra-pancreatic ganglia [25]. Green: nuclear staining. (c, d) PanIN-lymphatic network association in surgical biopsy acquired from PDAC treatment. c: high-grade PanIN in tumor bulk (male/age, 67 years/T3N0). d: low-grade PanIN 5 cm distal to the tumor bulk. In c, 2-D image (inset i and ii) and 3-D projection (inset iii) identify the lymphatic network around the high-grade PanIN lesion. Blue: islets (glucagon staining). In d, white arrows (inset i) indicate the lymphatic vessels in the stroma. Blue arrows in inset ii specify the cell bodies of endothelium, confirming the thin-walled lymphatic vessels. Yellow arrows in c and d indicate the areas with aggregation of nuclear signals (inflammation), which appears to be associated with the lymphatic network. Note that acinar atrophy and mixed-grade PanINs are commonly found in the lobules distal to the tumor bulk. Supplementary Fig. S1 (male/age, 52 years/T2N0) shows a second example of the distal PanIN-lymphatic network association.

To establish the syngeneic mouse model of pancreatic tumor, we developed a PDAC cell line (clone Pan18) from the pancreatic tumors in the EKP mice (induced with tamoxifen and cerulein injections described above). In the process, the EKP tumors were dissected and treated with the digestion solution (10 mM HEPES, 1 mg/ml collagenase P, 1 U/ml Dispase, and 2.5 mM $CaCl_2$) to disassociate the tumor cells. The cells were then seeded in low density and cultured in DMEM with 4.5 g/L glucose, 100 U/ml penicillin and streptomycin, and 10% fetal bovine serum to monitor their growth. Clone Pan18 was later picked, preserved, and magnified on the basis of its aggressive proliferation. Next, the Pan18 cells were labeled via transduction with the lentivirus carrying the IRES-based dual expression cassette of luciferase (for in vivo monitoring/confirmation) and EGFP (for cell tracing) and then purified three times with the FACSAria II cell sorter (BD Biosciences, San Jose, CA, USA) to select the EGFP^{+} cells. Finally, to engraft the tumor cells, ~1 × 10^3 EGFP^{+} Pan18 cells in Matrigel (40 μl; BD Biosciences) were injected to the B6 mouse pancreas (6–8 weeks of age) through an abdominal incision (control: injection of Matrigel only). Once the Matrigel solidified, the incision was closed with 0.1 mm (5/0) Safil absorbable surgical suture (B. Braun Medical, Barcelona, Spain). The development of the pancreatic tumors was monitored using the Xenogen IVIS Spectrum System (Caliper, Waltham, MA,

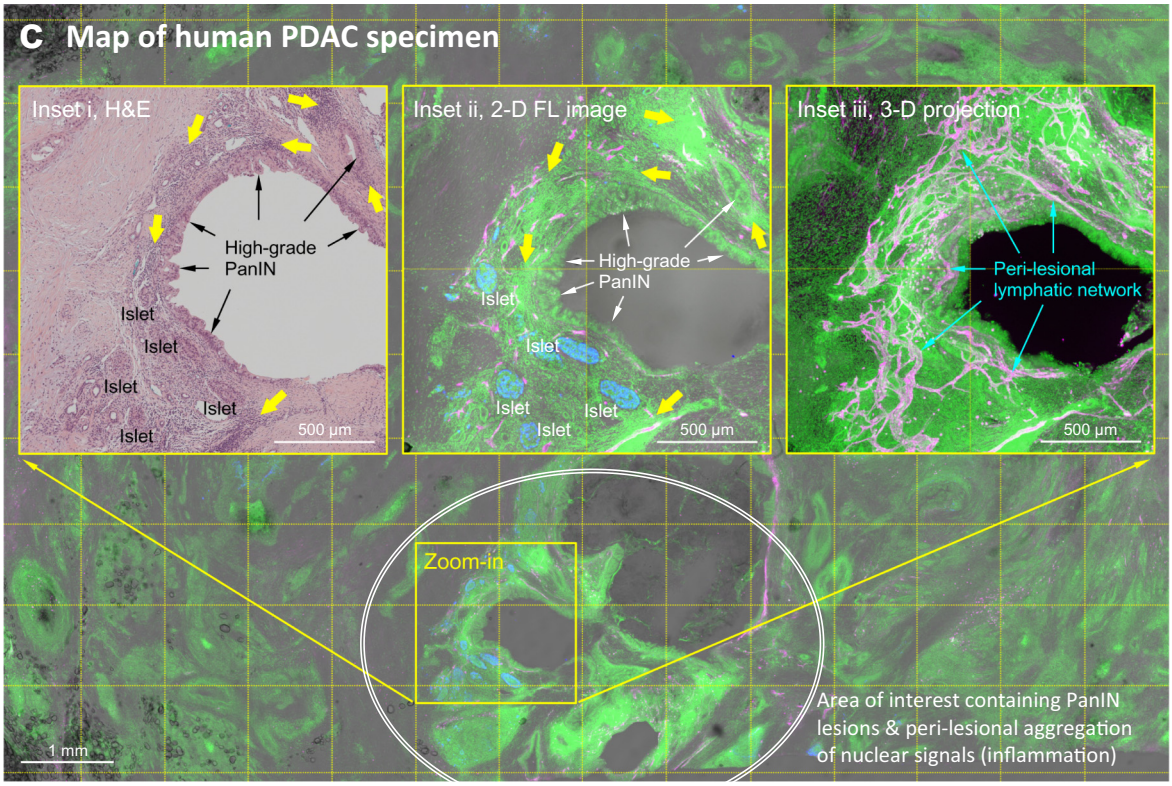

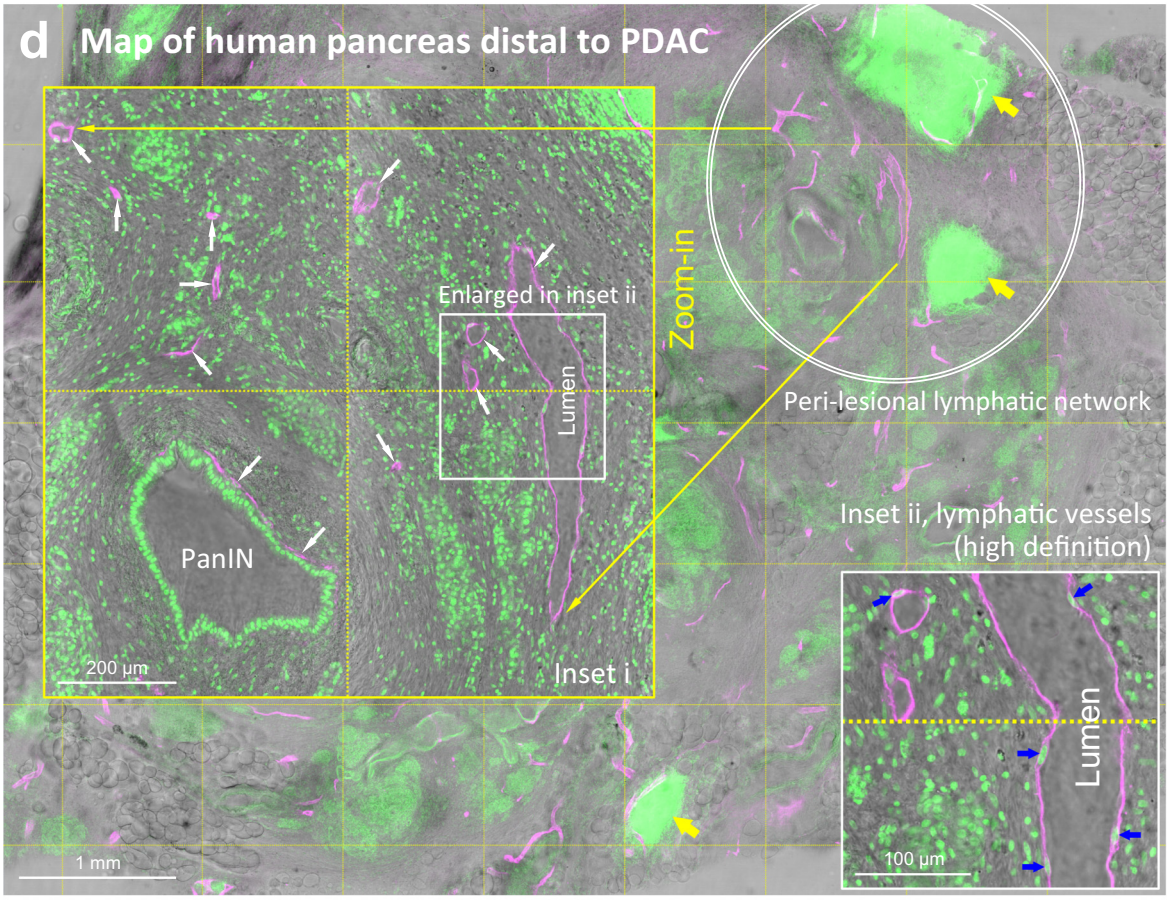

Fig. 1 (*continued*).

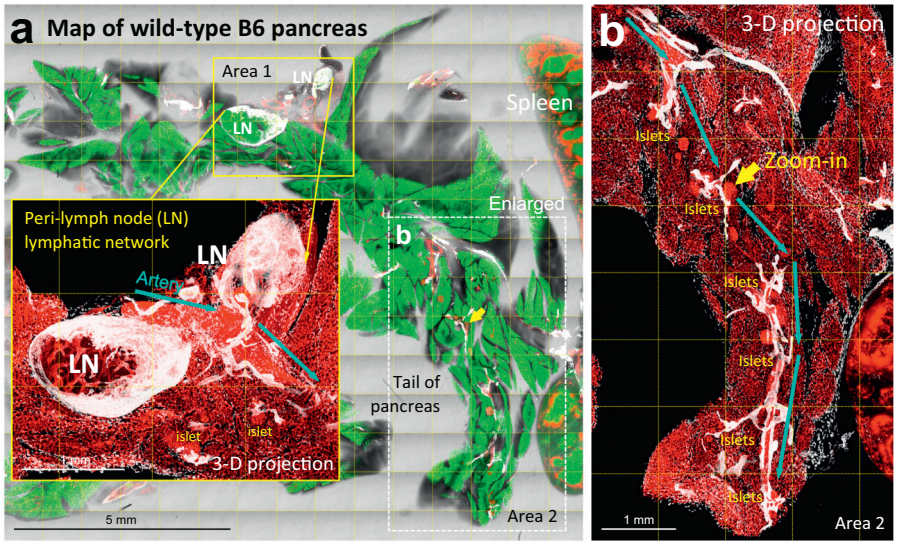

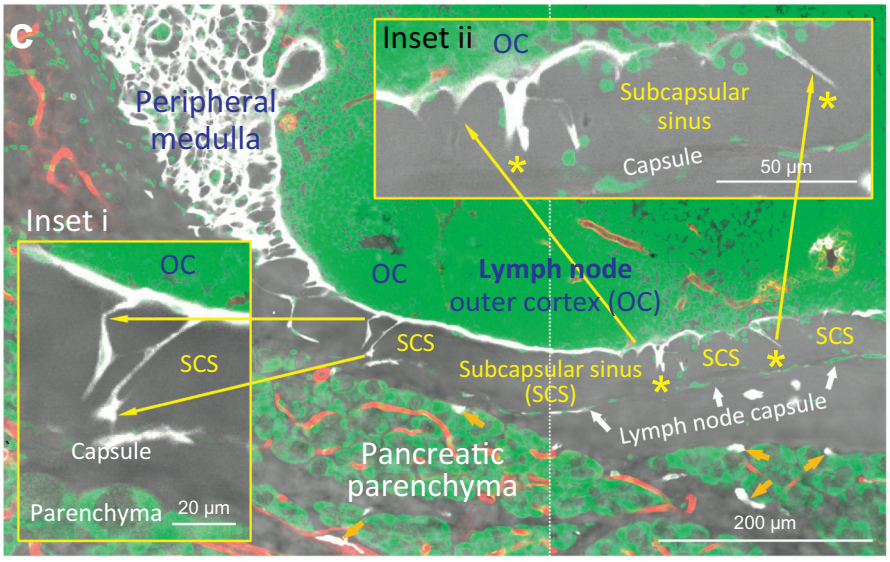

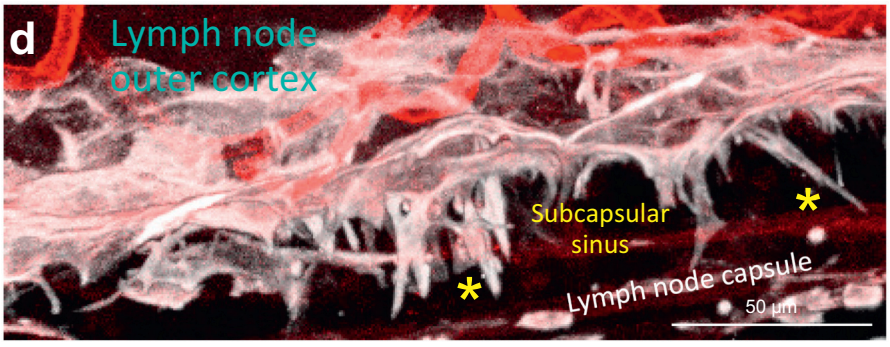

Enlarged projection of inset ii

Fig. 2. Mouse pancreatic lymphatic system. (a, b) Tissue map of wild-type B6 mouse pancreas labeled with lymphatic marker Lyve1. White: Lyve1. Red: blood vessels. Green: nuclear staining. Area 1 is enlarged (inset) to reveal the lymph nodes (LN) around the artery. Area 2 is enlarged in b to depict the extension of peri-arteriolar lymphatic network (cyan arrows) and the surrounding islets. Yellow arrow indicates the area enlarged in e. (c, d) Bridge-like endothelium across the subcapsular sinus of lymph node. 2-D image (c) and 3-D projection (d) of the subcapsular sinus (SCS) show that the Lyve1^{+} endothelium not only lines the floors of lymph node but also extend across the outer cortex and reach to the capsule (asterisks). (e) Microenvironment of lymphatic vessels in mouse pancreas. This image highlights the lympho-acinar and lympho-islet association and the wall-to-wall contact of lymphatic vessels with the arteriole, venule, and inter-lobular duct. Arrow indicates the association and extension of the lymphatic vessel (LV) and arteriole.

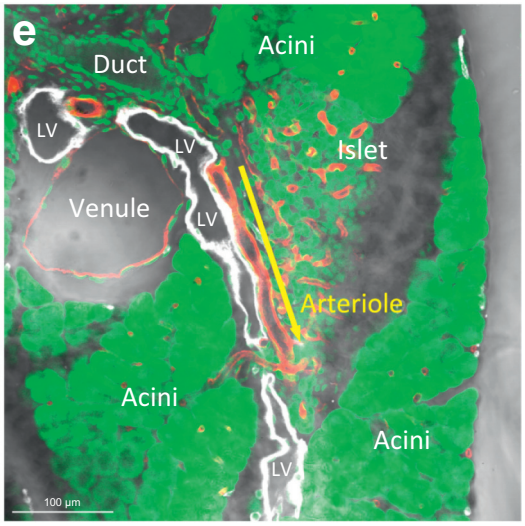

Fig. 2 (*continued*).

USA) for 1 month before killing the animals for examination. Six Pan18-injected and four control mice were examined with 3-D histology to characterize the tumor cell-induced lymphangiogenesis and lymphatic vessel invasion.

Mouse pancreatic blood vessels were labeled with cardiac perfusion of the lectin-Alexa Fluor 488 conjugate (Invitrogen, Carlsbad, CA, USA) followed by 4% paraformaldehyde perfusion fixation [26]. Afterward, the pancreas was harvested and post-fixed in 4% paraformaldehyde solution for 40 min at 15 °C. Vibratome sections of the fixed pancreas were then prepared and the sections were transferred to 0.1% paraformaldehyde for preservation at 4 °C. The Institutional Animal Care and Use Committees at the Academia Sinica and the National Tsing Hua University approved all procedures with mice.

2.3. Tissue immunolabeling

The fixed human and mouse specimens were immersed in 2% Triton X-100 solution for 2 h at 15 °C for permeabilization before immunolabeling. Eight different primary antibodies were used to immunolabel the tissues following the protocol outlined below. For human tissue labeling, the antibodies used were mouse anti-podoplanin (clone D2-40, lymphatic endothelial marker; 916602, BioLegend, San Diego, CA, USA) [27,28], rabbit anti-PGP9.5 (neuroendocrine marker; 2932–1, Epitomics, Burlingame, CA, USA) [25], rabbit anti-glucagon (2810–1, Epitomics), and rabbit anti-α-SMA (stellate cell marker; ab5694, Abcam, Cambridge, MA, USA). For mouse tissue labeling, the antibodies used were rabbit anti-lymphatic vessel endothelial hyaluronan receptor 1 (Lyve1, lymphatic vessel endothelial marker; Lyve1 staining also labels a subpopulation of macrophages; ab14917, Abcam), rat-anti-substance P (sensory nerve marker, MAB356, Millipore, Billerica, MA, USA), rabbit anti-Ki-67 (cell proliferation marker; ab15580, Abcam), and mouse anti-nestin (cancer stem cell marker, MAB353, Millipore) [29] antibodies. Before applying the antibody, the tissue was rinsed in phosphate-buffered saline (PBS). This was followed by a blocking step, incubating the tissue with the blocking buffer (2% Triton X-100, 10% normal goat serum, and 0.02% sodium azide in PBS). The primary antibody was then diluted in the dilution buffer (1:100, 0.25% Triton X-100, 1% normal goat serum, and 0.02% sodium azide in PBS) to replace the blocking buffer and incubated for 1 day at 15 °C. Negative controls were prepared by omitting the primary antibody in the buffer.

Alexa Fluor 647 conjugated goat anti-rabbit secondary antibody was used in combination with Alexa Fluor 546 conjugated goat anti-mouse or anti-rat secondary antibody (1:200, Invitrogen) to reveal the immunostained structures. Propidium iodide or SYTO 16 (Invitrogen) staining was performed at room temperature for 1 h to reveal the nuclei. The labeled specimens were then immersed in the tissue clearing solution (RapiClear 1.52 solution, SunJin Lab, Hsinchu, Taiwan) before being imaged via confocal microscopy.

2.4. Deep-tissue confocal microscopy

Imaging of the tissue structure was performed with Zeiss LSM 510 Meta or LSM 800 confocal microscope (Carl Zeiss, Jena, Germany) equipped with 10× Fluar lenses and 25× LD Plan-Apochromat lenses (working distance: 570 μm) under a tile-scan mode with automatic image stitching. The laser-scanning process was operated under the multi-track scanning mode to acquire signals, including the transmitted light signals. The Alexa Fluor 647-labeled structures were excited at 633 nm and the fluorescence was collected by the 650–710-nm band-pass filter. The propidium iodide-labeled nuclei and Alexa Fluor 546-labeled structures were excited at 543 nm and the signals were collected by the 560–615-nm band-pass filter. The SYTO 16-labeled nuclei and lectin-Alexa Fluor 488-labeled blood vessels were excited at 488 nm and the fluorescence was collected by the 500–550-nm band-pass filter. Fluorescence signals in figures are pseudo-colored. After confocal imaging, the specimens were further processed with saline washing (removal of clearing reagent) and H&E histology to confirm the PanIN structure (e.g., Fig. 1c) if necessary.

2.5. Image projection and analysis

The Avizo 6.2 image reconstruction software (VSG, Burlington, MA, USA), Zen software (Carl Zeiss), and LSM 510 software (Carl Zeiss) were used for projection, signal segmentation, noise reduction, and analysis of the confocal images. Signal segmentation for quantification of the tissue network (or cell) density is illustrated in Juang et al. [30]. Briefly, feature extraction and image segmentation for calculation of the lymphatic vessel density were performed by the Label Field function of Avizo to collect the voxels of the area of interest (parenchyma, lesion, or peri-lobular space; the last one is within 500 μm off the edges of lobules, excluding the intra-lobular signals) and the associated Lyve1$^+$ lymphatic vessels. Voxels of the vessels were divided by those of the area of interest ×100% to estimate the lymphatic vessel density. Quantitation of the Lyve1$^+$ macrophage density follows the same approach except that the cell numbers instead of the voxels were used in the numerator, and the voxels of the lesion, peri-lesional parenchyma (within 500 μm of the lesion), or normal parenchyma were used in the denominator. The same immunolabeling, imaging, and quantitation processes were conducted on the comparable pancreatic middle sections to characterize the tissue densities on the same basis.

2.6. Statistical analysis

The quantitative values are presented as means ± SD or with the distribution of data points. Statistical differences were determined by the unpaired Student's *t*-test. Differences between groups were considered statistically significant when $P < .05$.

3. Results

3.1. Human pancreatic lymphatic network in health and around PanIN lesions

The pancreas consists of the endocrine islets and the exocrine acini and ductal network to control and participate in the body's metabolic and digestive activities. From the map of human pancreas (Fig. 1a, b), we see both the endocrine and exocrine tissues and the infiltrated adipocytes contact with the podoplanin (D2-40) -labeled lymphatic

network [27]. The association underscores the surveillance feature of lymphatics. Note that we used tissue clearing to prepare transparent human pancreases for penetrative 3-D imaging [24,25]. The transparent specimens allowed us to use both the transmitted light and fluorescence signals to identify and confirm the pancreatic microstructure and tissue networks (ducts, nerves, and vasculature) in space.

Importantly, in addition to the normal pancreas, this 3-D imaging approach can be used to examine the human pancreatic cancer specimens with high definition. Fig. 1c shows the map of a human PDAC tissue acquired from pancreatectomy. Deposits of high-grade PanIN lesions are detected in the tumor bulk with tissue scanning. In the map, patches of nuclear signals highlight the inflammatory areas, which are associated with the PanIN lesions. A side-by-side comparison of the H&E and fluorescence micrographs identifies the close association between the high-grade PanINs and the lymphatic network (insets of Fig. 1c and Supplementary Video S1). In addition, in the diseased pancreas distal to the tumor bulk (Fig. 1d and Supplementary Fig. S1), the lesion (low grade) -lymphatic vessel association is also seen in the lobule with apparent acinar atrophy (vs. Fig. 1a; $n = 3$ surgical biopsies).

Although the human PDAC analysis provides direct evidence of the lesion-lymphatic network association, it does not allow us to trace the development of the association, which requires examination of the PanIN lesions at their early stage (i.e., when the pancreas appears to be normal) as well as the advanced stage. In the next six sections we systematically analyze the mouse PanIN and PDAC models to characterize the lymphatic vessel remodeling and invasion in pancreatic duct lesion progression.

3.2. Mouse pancreatic lymphatic system detected by 3-D histology

Similar to the human pancreatic lymphatic system [2], the mouse pancreatic lymph nodes reside in the peri-lobular space and around the artery (Fig. 2a, Area 1). In mice, the lymph nodes and lymphatic vessels are visualized with Lyve1 (lymphatic vessel endothelial hyaluronan receptor 1) staining of the lymphatic endothelium [31–33] (note that Lyve1 also labels a subpopulation of F4/80$^+$ macrophages, Supplementary Fig. S2 [34,35]). Morphologically, outside the lymph node, the Lyve1$^+$ endothelium forms a torturous network which follows the artery and arteriole in extension (Fig. 2a, inset, and b). Inside the lymph node, the Lyve1$^+$ endothelium lines the floors of the medullary and subcapsular sinuses (Fig. 2c; positive control of Lyve1 staining) [36]. Interesting, although the endothelial lining of the lymph node has been known, its extension across the subcapsular space has not been reported (Fig. 2c, insets, and d). This unique bridge structure is only seen inside the lymph node in normal mice but appears outside the lymph node in lymphangiogenesis, which will be discussed later.

Zooming out from the lymph node, Fig. 2e presents the high-definition image of an inter-lobular lymphatic vessel, which resides at the central location among the pancreatic lobules. This image shows the contact of lymphatic endothelium with all of the pancreatic major structures, including the endocrine islets, exocrine acini and ducts, and blood vessels (arterioles and venules). The association is comparable to that of the lymphatic network in the human pancreas (Fig. 1a).

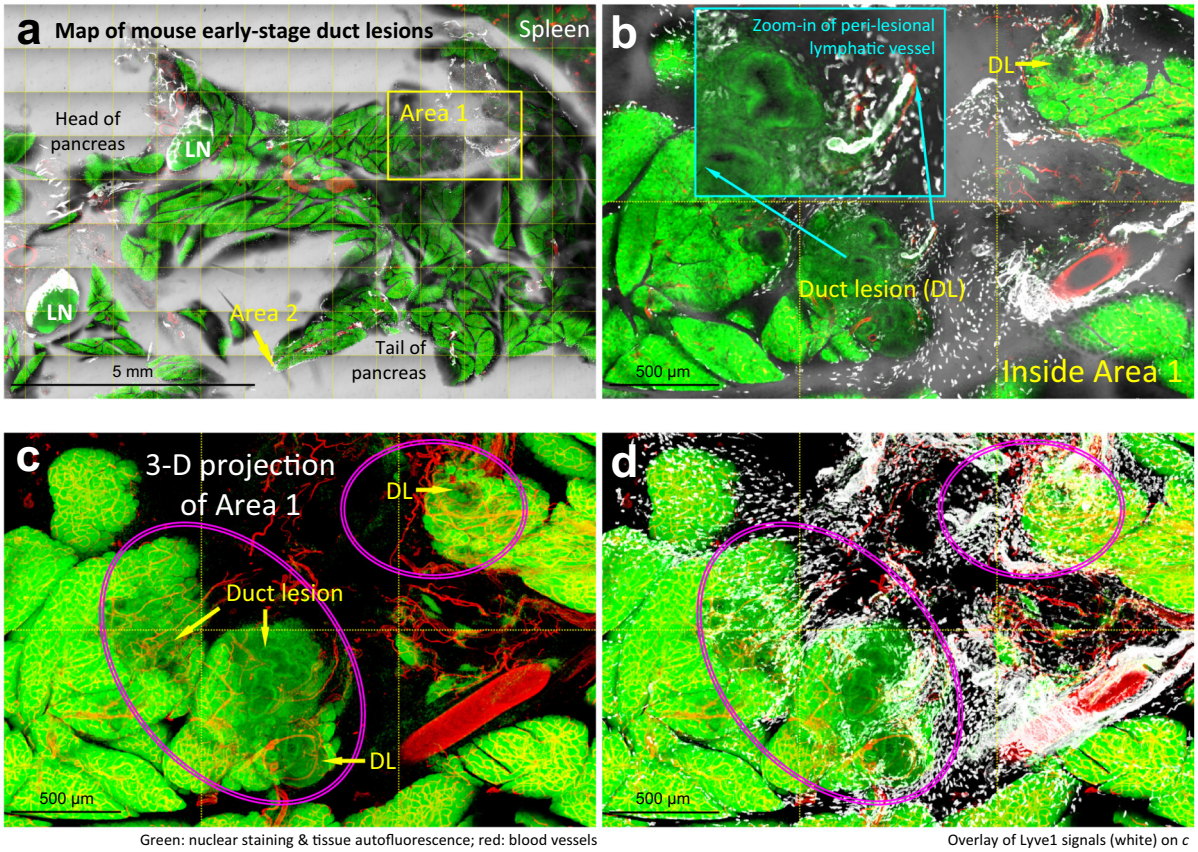

Fig. 3. Lymphangiogenesis and macrophage accumulation in early-stage duct lesion formation. (a) Tissue map of EK mouse pancreas labeled with lymphatic marker Lyve1. White: Lyve1. Red: blood vessels. Green: nuclear staining. The box (Area 1) and arrow (Area 2) indicate early-stage duct lesions (enlarged in b-d and e–g). (b–g) Peri-lesional lymphangiogenesis and aggregation of Lyve1$^+$ macrophages. b–d, gross view. Duct lesions (DL) are highlighted by arrows and ovals. Lymphangiogenesis (inset in b) and accumulation of Lyve1$^+$ macrophages (white dots in b and d) are identified in the peri-lesional region. b: 2-D image. c, d: 3-D projections (depth: 120 μm). e–g: high-definition images of duct lesion. Note that the early lesions often occur at the edge of parenchyma. Supplementary Fig. S3 provides an additional example of the early-stage duct lesion with high definition. (h, i) Increase in Lyve1$^+$ macrophages and lymphatic vessel density around the early-stage duct lesions. Peri-lesional parenchyma is arbitrarily defined as the parenchyma within 500 μm of the lesion. Data are presented as mean ± SD ($n = 4$ mice; $^*P < .05$; $^{**}P < .01$).

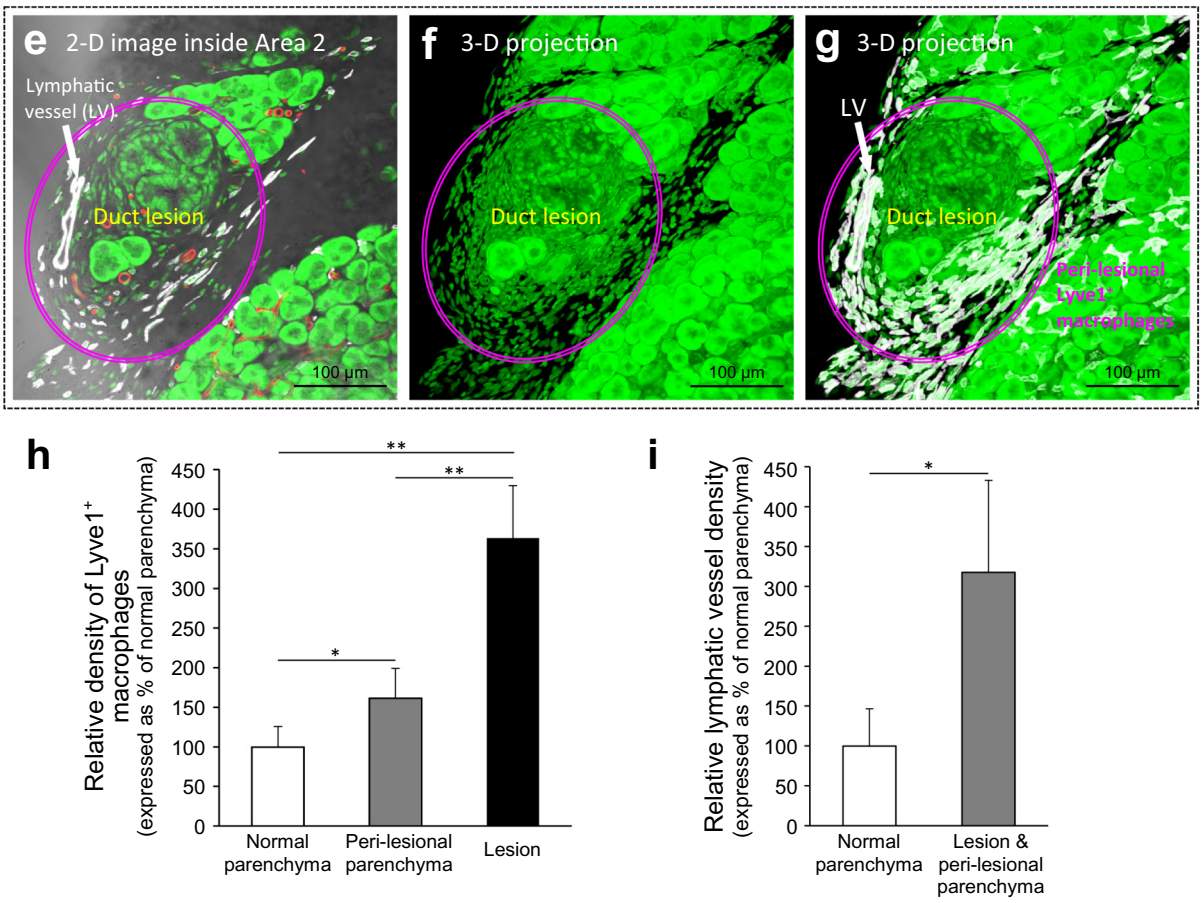

Fig. 3 (*continued*).

3.3. Lymphangiogenesis and macrophage accumulation in early-stage duct lesion formation

Oncogenic *Kras* mutation often occurs in human PDAC [9,37]. Experimentally we used *elastase-Cre*ER;LSL-*Kras*^{G12D} mice (EK mice) to induce acinar oncogenic *Kras* expression, which causes acinar-to-ductal metaplasia and spontaneous induction of PanIN lesions (PanIN-1/2) to mimic the human condition [13,18]. Fig. 3a shows a gross view of the EK mouse pancreas at the early stage of duct lesion formation. At this stage, the majority of parenchyma (~98%) is anatomically normal [18]. However, scattered PanIN lesions appear at the edges of parenchyma, such as in Area 1 and 2 in Fig. 3a, which are enlarged in Fig. 3b–d and e–g for examination.

Specifically, the 2-D images and 3-D projections of the early-stage duct lesions identify the formation of peri-lesional lymphatic vessels (Fig. 3b, c, and Supplementary Fig. S3), which is confirmed by the paired Prox1 and Lyve1 staining (Supplementary Fig. S4), and the accumulation of Lyve1$^+$ macrophages around the lesion (Fig. 3d, g). Quantitation of the Lyve1$^+$ signals shows 61% ($P < .05$) and 263% ($P < .01$) increases in the density of Lyve1$^+$ macrophages in the peri-lesional parenchyma and the lesion area, respectively, and a 218% ($P < .05$) increase in lymphatic vessel density of the influenced area, suggesting an ongoing inflammatory response around the lesion (Fig. 3h, i).

3.4. Lymphangiogenesis, endothelial invagination, and vessel invasion in large-scale duct lesion formation

We next used 3 weeks of cerulein injections to create repetitive pancreatic injuries (pancreatitis) and followed with 4 weeks of tissue regrowth to induce aggressive epithelial proliferation and large-scale duct lesion formation [18]. Fig. 4a–d presents the remodeling of the pancreatic microstructure and lymphatic network in this condition. Morphologically, the tissue injury and epithelial overgrowth lead to acinar atrophy and lesion/stromal adhesion to the surrounding organs, such as the intestine (Fig. 4d). This tissue remodeling is accompanied with marked lymphangiogenesis, in which the Lyve1$^+$ endothelium occupies the peri-lobular space and extends along the interface between the lesion and the attached tissues, such as the lymph node (Area 1 in Fig. 4a; enlarged in Fig. 4b, c and Supplementary Video S2) and the intestinal serosa (Area 2 in Fig. 4a; enlarged in Fig. 4d). These drastic changes, however, are not seen in the wild-type B6 mice which went through the same process of 3-week cerulein pancreatitis and 4-week tissue regrowth (Supplementary Fig. S5). The B6 pancreas regenerates without apparent microstructural and lymphatic network remodeling, confirming that the genetic predisposition in the EK mice is essential for the large-scale duct lesion formation and the associated lymphangiogenesis.

Furthermore, when the large-scale duct lesion formation is induced under the background of *p53* mutation (*elastase-Cre*ER;LSL-*Kras*^{G12D}; *p53*$^{+/-}$, the EKP mice) [38], we identify the lymphatic luminal invasion in five of the seven examined animals (Fig. 4e–i). Histologically, the lymphatic luminal invasion has the following two features: (i) it occurs at the peri-lobular spaces with lymphangiogenesis (Fig. 4e, f, and Supplementary Fig. S6), and (ii) it is associated with invagination of the Lyve1$^+$ endothelium (Fig. 4f, g, and Supplementary Fig. S7).

Quantitation of the Lyve1$^+$ signals shows that the density of the pancreatic lymphatic vessels in the EK and EKP mice increases 5.5-fold ($P < .01$) and 4.9-fold ($P < .01$) against the wild-type B6 mice,

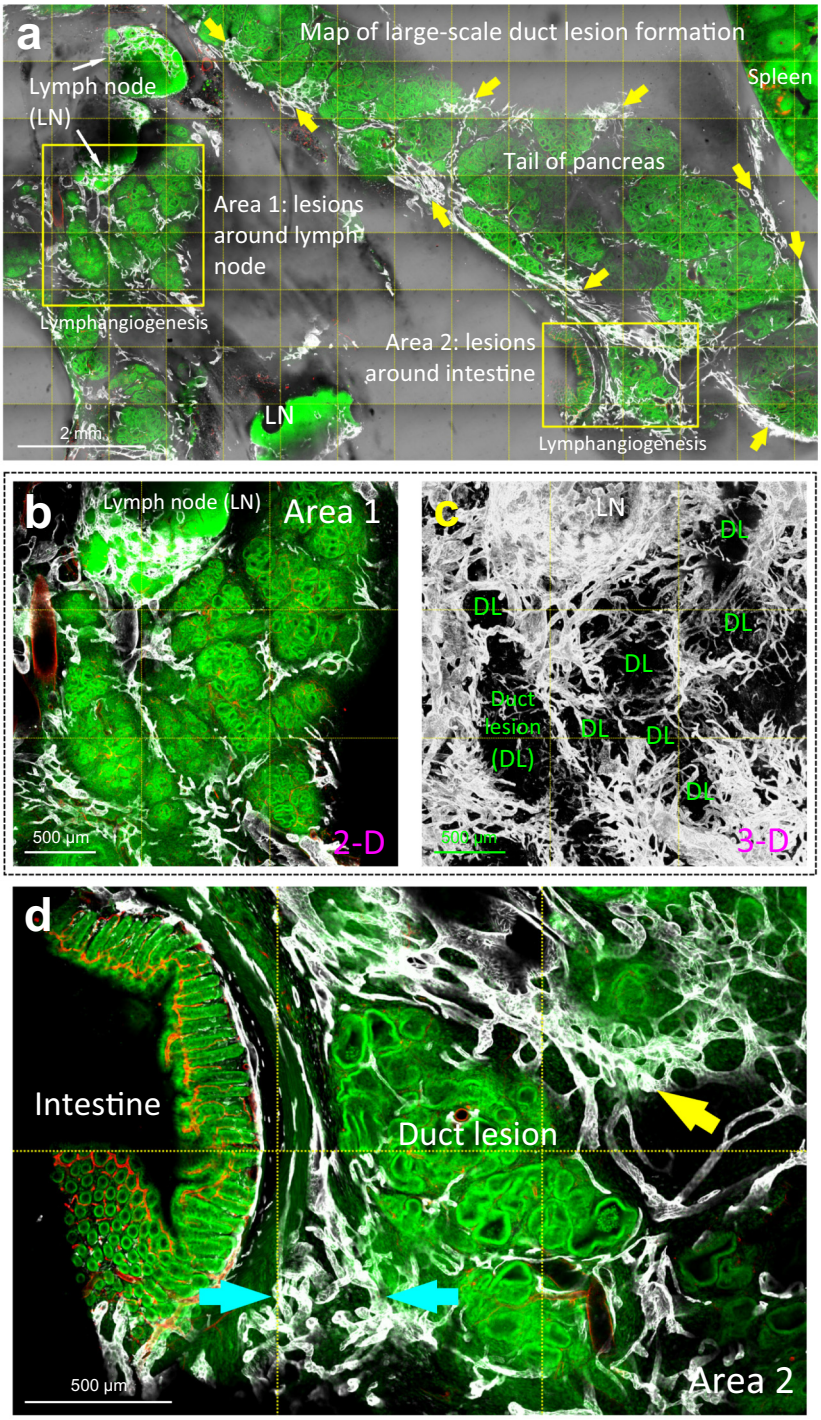

Fig. 4. Lymphangiogenesis and luminal invasion in large-scale duct lesion formation. (a) Tissue map of EK mice treated with cerulein to induce large-scale duct lesion formation (PanIN-1/2). White: Lyve1. Red: blood vessels. Green: nuclear staining. Condensed lymphatic vessels are prominently seen at the peri-lobular region (yellow arrows). Lymphangiogenesis around the lymph node (Area 1) and the lesion-intestinal boundary (Area 2) are enlarged in b–d. (b, c) Gross view of peri-lesional lymphangiogenesis nearby a lymph node. LN: lymph node. DL: duct lesion. (d) Lymphangiogenesis around PanIN lesions attached to intestinal serosa. Cyan arrows: abnormal network integration at the organ boundary. Yellow arrow: peri-lobular lymphangiogenesis. (e–g) Endothelial invagination and luminal invasion in EKP mice. e: tissue map. The yellow box is enlarged in f. f and g present two examples of the peri-lesional endothelial invagination. Arrows indicate the cavities and pouches formed by the Lyve1^{+} endothelium via invagination. Note that cells are found inside the invaginated area (such as daggers in g). L: lumen of lymphatic vessel. (h) Quantitation of lymphangiogenesis in large-scale duct lesion formation. Both EK and EKP mice show a drastic increase in the peri-lobular lymphatic vessel density after cerulein treatment and tissue regrowth (no statistical difference between EK and EKP mice). There is no statistical difference between the normal B6 mice and the cerulein-treated B6 mice after tissue regrowth. Data are presented as mean ± SD ($n = 5$; $^{**}P < .01$ vs normal B6; $^{\dagger\dagger}P < .01$ vs cerulein-treated B6). (i) Detection of lymphatic luminal invasion, EK vs. EKP mice. 57% increase in the frequency of luminal invasion was observed in the EKP mice compared with the EK mice ($n = 7$). Two comparable pancreatic sections (~50 mm^3) from each animal were used in h and i.

respectively. However, there is no statistical difference between the EK and EKP mice in the level of lymphangiogenesis (Fig. 4h), indicating that the increased incidence of the luminal invasion in the EKP mice compared with the EK mice (Fig. 4i) is likely due to the behavioral changes of the lesion and/or stromal cells, rather than the probability of contacts between the lesions and lymphatic vessels.

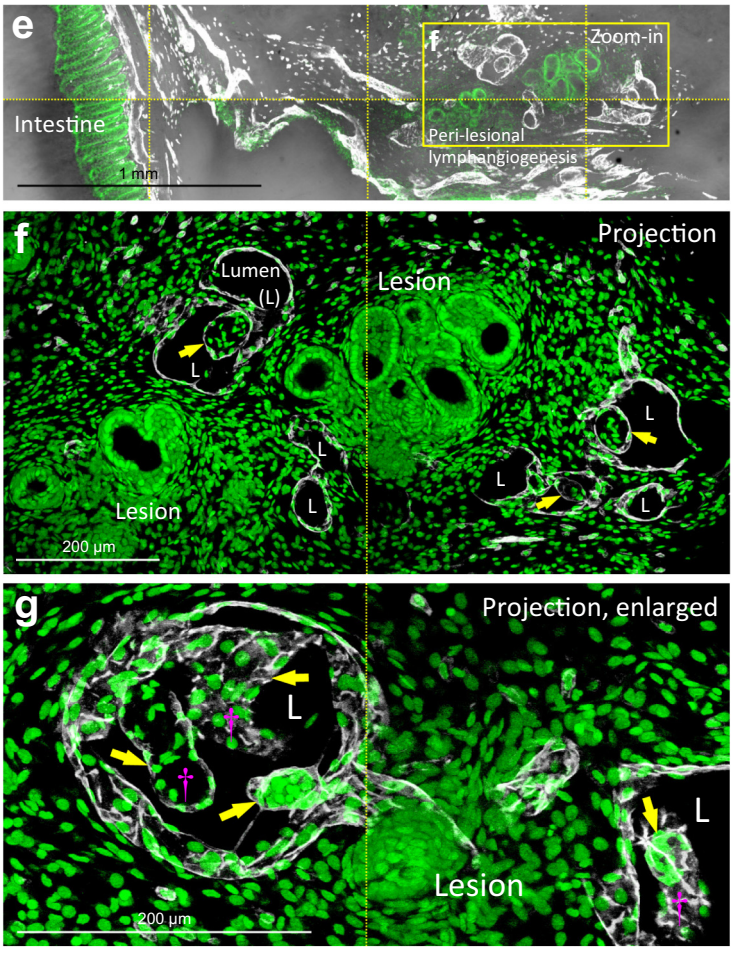

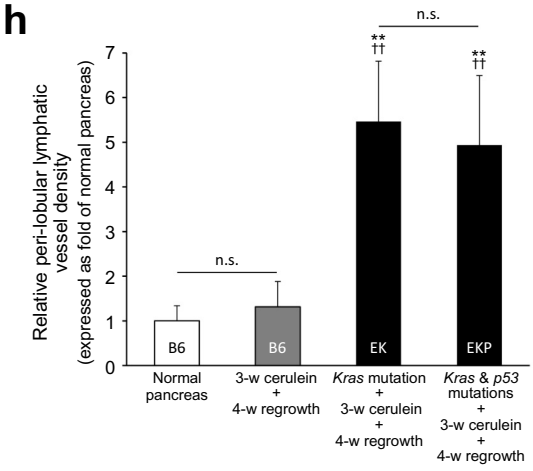

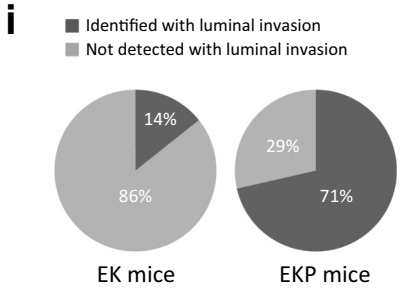

Fig. 4 (*continued*).

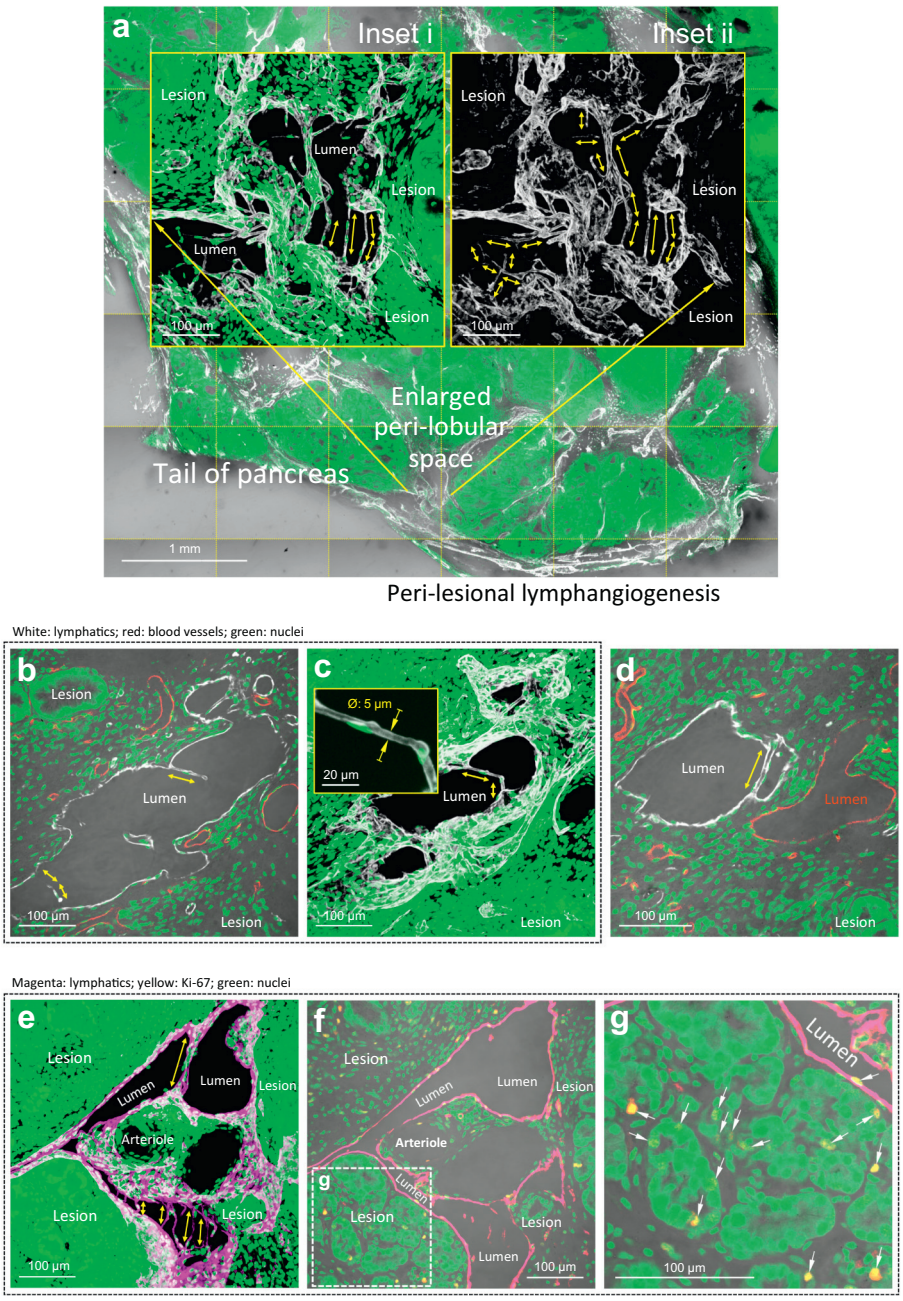

Fig. 5. Formation of lymphatic luminal tubules in lymphangiogenesis. (a) Tissue map and projection of lymphatic luminal tubules. An area of the peri-lobular space in the EKP mice is enlarged in inset i and ii (projections) to illustrate the bridge/valve-like tubules (double-headed arrows). Inset i (Lyve1, white; nuclei, green) and inset ii (Lyve1 only) focus at the same location. (b–d) High-definition images of lymphatic luminal tubules. b and c are 2-D image and 3-D projection of the tubules (diameter at ~5 μm, inset in c). d compares the peri-lesional blood vessel (red) and lymphatic vessel (white). Only the latter is found with the luminal tubule. (e–g) Joint events of peri-lesional lymphangiogenesis, lymphatic tubule formation, and cellular proliferation. Paired Lyve1 and Ki-67 staining confirms that the tubule formation occurs in a proliferative microenvironment. Arrows in g indicate the Ki-67$^+$ proliferating cells. Magenta: Lyve1. Yellow: Ki-67$^+$ nuclei. Green: nuclei.

3.5. Formation of luminal bridge/valve-like tubules in lymphangiogenesis

In lymphangiogenesis in the EK and EKP mice, the lymphatic endothelium extends from the central area of the parenchymas (Fig. 2a) to the peri-lobular space (Fig. 4a, e), forming a tube network (Supplementary Fig. S7). Interestingly, inside the tube network, the endothelial expansion is accompanied with formation of the bridge/valve-like structures, or *tubules* (with a diameter at ~5 μm), across the walls of the Lyve1$^+$ endothelium (Fig. 5a–e). The geometric feature of the tubules resembles the Lyve1$^+$ endothelium in the subcapsular space (sinus) of the lymph node in the normal mice (Fig. 2c, d).

To visualize the lymph node and the nearby duct lesions in a continuous fashion, Supplementary Video S3 presents the Lyve1$^+$ tubules in the EKP mice, which extend across the subcapsular sinus of the lymph node and bridge the peri-lobular space of the pancreas. The detection of the luminal tubules indicates the creation of the internal structure (frames/valves) as well as the walls of lymphatic vessels in the marked lymphangiogenesis in the EK and EKP pancreases. Furthermore, using the paired Lyve1 and Ki-67 staining, we confirm that the formation of the lymphatic luminal tubules, lymphangiogenesis, and cellular proliferation are parallel events (Fig. 5e–g). The Ki-67$^+$ cells are identified in the lesion, stroma, and wall of lymphatic vessel.

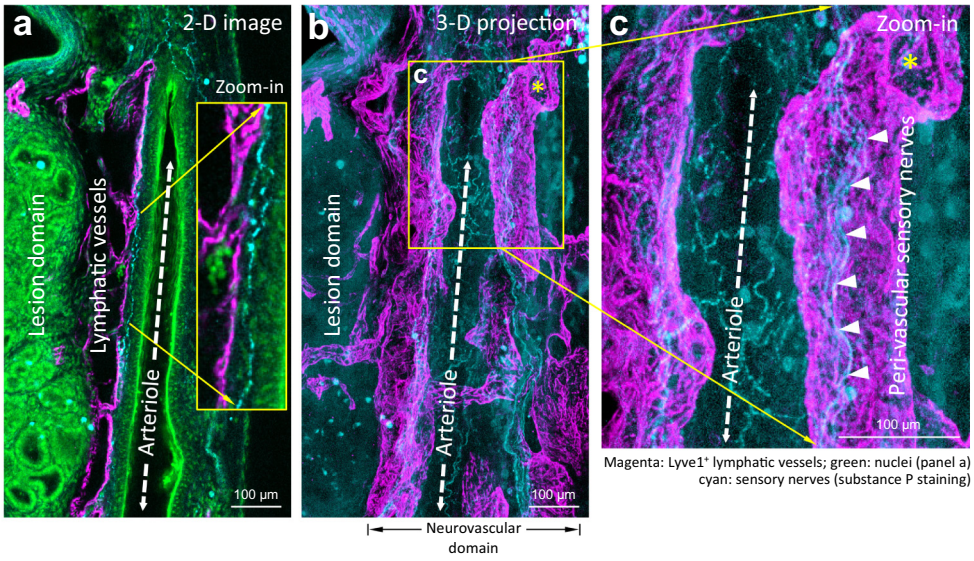

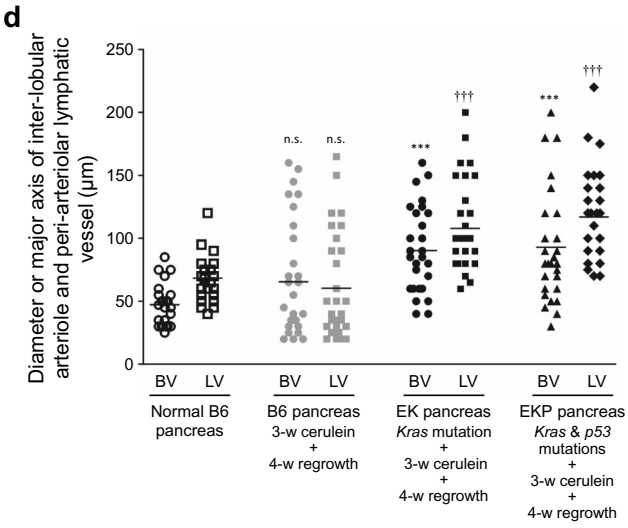

Fig. 6. Lymphatic vasodilation in large-scale duct lesion formation. (a, b) 2-D image and 3-D projection of peri-lesional neurovascular association in EKP mice. Substance P^+ sensory nerves (cyan) are identified along the path of the peri-lesional arteriole (dashed double-headed arrow) and lymphatic vessel (magenta). Green: nuclear staining. (c) High-definition 3-D projection of the neurolymphatic complex. Asterisks in b and c indicate the same opening of the lymphatic vessel. Arrow heads: substance P^+ sensory nerves. (d) Quantitation of vasodilation in large-scale duct lesion formation. Inter-lobular arterioles (BV) and peri-arteriolar lymphatic vessels (LV) were analyzed in four normal B6 mice (24 locations) and five B6, EK, and EKP mice after cerulein treatment and tissue regrowth (30 locations each). n.s. (not significant), $^{***}P < .001$, $^{\dagger\dagger\dagger}P < .001$ vs normal B6.

3.6. Lymphatic vasodilation in large-scale duct lesion formation

Among the reactive vascular responses in large-scale duct lesion formation, vasodilation is a prominent feature in the PanIN microenvironment. In the EKP mice, Fig. 6a–c shows the peri-lesional association among the inter-lobular arteriole, the peri-arteriolar lymphatic vessels, and the sensory nerves (labeled with substance P) [39]. In particular, the magnified 2-D image and 3-D projection of sensory nerves identify their contacts with the two vascular systems. The result indicates the vascular sensory innervation and the likely influence of the neuromodulators/neurotransmitters (e.g., substance P) on the microvessels. Quantitative analysis shows a 91% ($P < .001$) and 98% ($P < .001$) increase in the arteriolar diameter and a 59% ($P < .001$) and 72% ($P < .001$) increase in the major axis of the peri-arteriolar lymphatic vessels in the EK and EKP mice, respectively, in the cerulein-induced large-scale duct lesion formation (Fig. 6d). There is no significant difference in the B6 pancreatic microstructure and vasculature 4 weeks post the cerulein treatment compared with those of the untreated pancreas (Supplementary Fig. S5).

3.7. Lymphatic vessel invasion in syngeneic mouse model of orthotopic cancer cell injection

To mimic the localized pancreatic lymphatic vessel invasion (vs. generalized pancreatic remodeling in EK and EKP mice, Fig. 4), we used the orthotopic injection of the syngeneic, $EGFP^+$ pancreatic cancer cells to trace their location and association with lymphatic vessels via 3-D imaging. Fig. 7a shows the tumor formed locally around the pancreatic parenchyma and the peri-tumoral lymphangiogenesis induced by the cancer cell injection. Specifically, in the peri-tumoral domain, clusters of the invading cells were found inside the $Lyve1^+$ lymphatic vessels with few cells appearing >500 μm distal to the tumor domain (Fig. 7a, insets), indicating an ongoing spread of cancer cells. Furthermore, Supplementary Fig. S8 presents the budding of $EGFP^+$ cells against the lymphatic endothelium, highlighting the vascular plasticity and the invasive nature of injected cancer cells.

Surprisingly, using the panoramic tumor scan, we identify that the lymphangiogenesis and lymphatic vessel invasion are not limited to

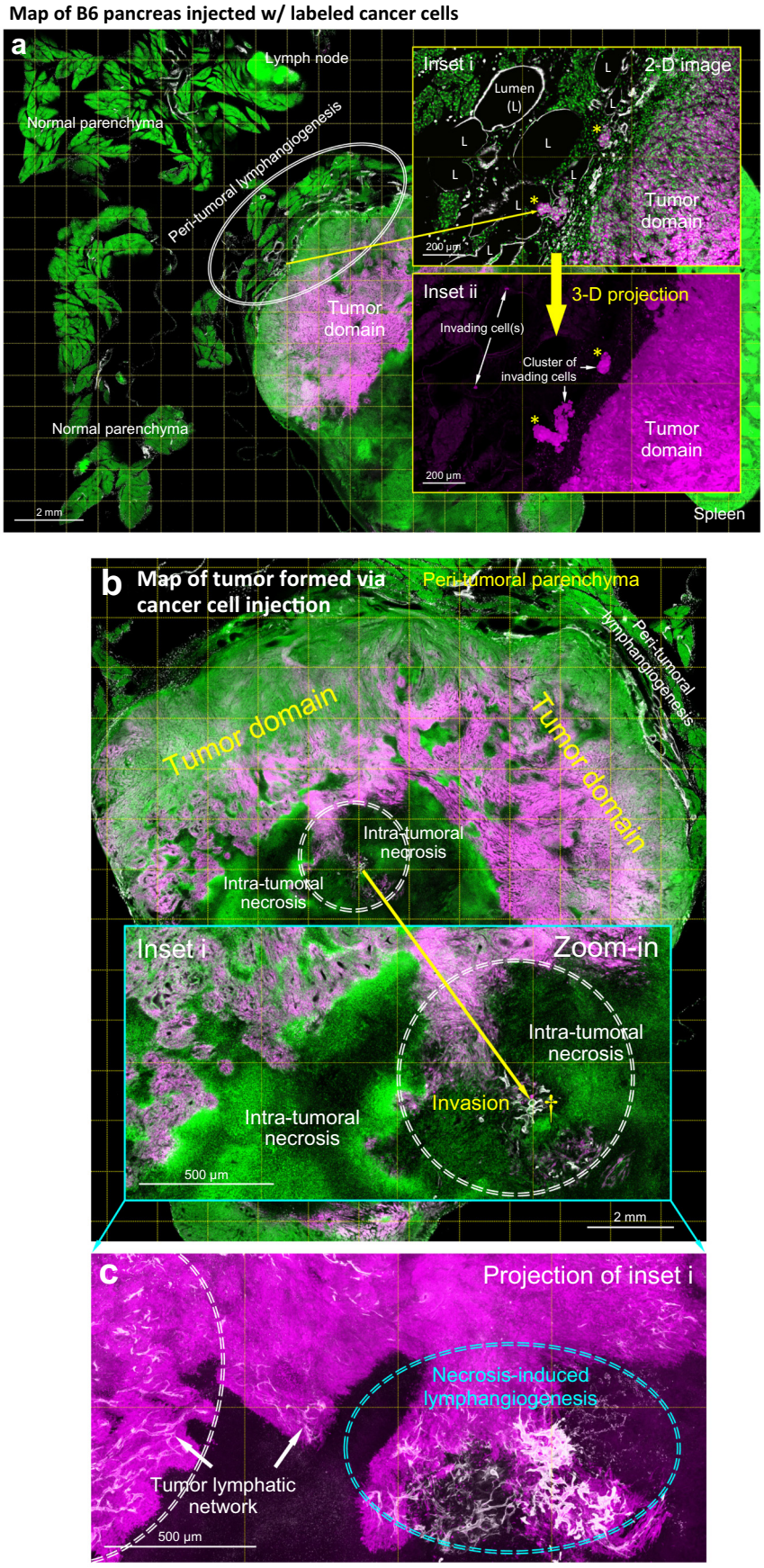
Map of B6 pancreas injected w/ labeled cancer cells
a
Lymph node
Normal parenchyma
Peri-tumoral lymphangiogenesis
Tumor domain
Normal parenchyma
2 mm
Inset i
2-D image
Lumen (L)
Tumor domain
200 μm
Inset ii
3-D projection
Invading cell(s)
Cluster of invading cells
Tumor domain
200 μm
Spleen
b
Map of tumor formed via cancer cell injection
Peri-tumoral parenchyma
Peri-tumoral lymphangiogenesis
Tumor domain
Tumor domain
Intra-tumoral necrosis
Intra-tumoral necrosis
Inset i
Zoom-in
Intra-tumoral necrosis
Invasion
Intra-tumoral necrosis
500 μm
2 mm
c
Projection of inset i
Necrosis-induced lymphangiogenesis
Tumor lymphatic network
500 μm

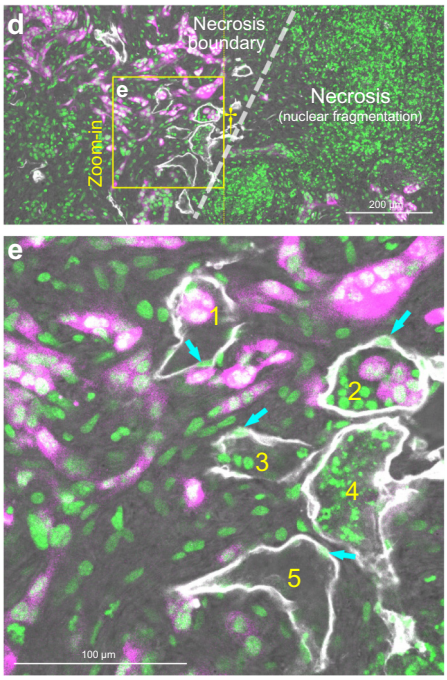

Fig. 7. Localized lymphangiogenesis and lymphatic vessel invasion in orthotopic EGFP$^+$ pancreatic cancer cell injection. (a) Peri-tumoral lymphangiogenesis and lymphatic vessel invasion. Injection of the cancer cell-Matrigel mixture induces lymphangiogenesis, which appears at the tumor-parenchymal boundary (oval; vs. normal parenchyma away from the tumor; $n = 6$ mice; note that Matrigel injection alone did not induce lymphangiogenesis, $n = 4$ mice). Enlarged 2-D image (inset i) and 3-D projection (inset ii) of the boundary reveal lymphatic vessel invasion (asterisks and white arrows). The invading cell clusters and cell(s) are identified in the lumen of lymphatic vessels. White: Lyve1. Magenta: EGFP$^+$ cancer cells. Green: nuclear staining. (b–e) Intra-tumoral necrosis, lymphangiogenesis, and lymphatic vessel invasion. b and c show the tumor map and the intra-tumoral area with necrosis and lymphangiogenesis (inset i, central area of the map; circle, area of interest). c is the projection of inset i in b. Cyan oval in c indicates the necrosis associated lymphangiogenesis. Lymphatic vessel invasion in this area is enlarged in d and e. d shows the microenvironment across the tumor necrosis boundary (dashed line; left, cells with intact nuclei; right, necrosis with nuclear fragmentation). Daggers in b and d indicate the same location. e shows the high-definition image of lymphatic vessel invasion (box in d). Numbers 1–5 indicate the five luminal conditions observed in this microenvironment. 1: labeled tumor cells. 2: labeled tumor cells and host cells (nuclei). 3: host cells. 4: nuclear fragments. 5: empty lumen. Cyan arrows: cell bodies of lymphatic endothelium.

the peri-tumoral domain. Inside the tumor, lymphangiogenesis is clearly seen associated with the necrosis in the tumor core (Fig. 7b, c). At the necrosis boundary (Fig. 7d), the endothelium-enclosed nuclear fragments and cancer cells (vessel invasion, Fig. 7e) are specified with high-definition 3-D microscopy (Supplementary Video S4). Quantitatively, the localized lymphangiogenesis and vessel invasion (peri- and/or intra-tumoral) are visualized in six of six (100%) and five of the six (83%) animals with the cancer cell injection, respectively. Overall, the 3-D image data provide novel details of the lymphatic vessel remodeling and invasion, which otherwise could not be illustrated using the standard 2-D histology.

4. Discussion

To overcome the difficulty of seeing the dispersed lymphatic network in space, in this research we combined panoramic and high-definition 3-D imaging to characterize the pancreatic lymphatic network in health and cancer progression. Using the human PDAC specimens, we demonstrated the association between the PanIN lesion and lymphatic network, establishing a clinically related setting for 3-D lymphatic network imaging (Fig. 1 and Supplementary Video S1). In experimental PanIN and PDAC, mutations (*Kras* or *Kras* and *p53*) and the cerulein-induced pancreatitis were systematically introduced to mice to investigate the early and advanced duct lesion formation. At the early stage (when the pancreas appeared to be normal), our 3-D imaging method detected the lesion-lymphatic vessel association and the peri-lesional accumulation of Lyve1$^+$ macrophages (Fig. 3). At the advanced stage (when duct lesions dominated the pancreas), we identified the widespread lymphangiogenesis (Fig. 4), which was accompanied with endothelial invagination and invasion (Fig. 4e–i), luminal bridge/valve-like tubule formation (Fig. 5), and vasodilation (Fig. 6). Finally, using the syngeneic orthotopic PDAC cell injection, we identified the localized lymphangiogenesis and vessel invasion in the peri- and intra-tumoral regions (Fig. 7). Overall, our 3-D image data indicate a highly plastic and dynamic lymphatic system that responds to the formation of pancreatic duct lesions with proliferation and remodeling.

Histologically, the invasive nature of pancreatic duct lesions is shown by the peri-lesional lymphatic vessel invasion with cell clusters (Figs. 4g, 7, and Supplementary Fig. S6; epithelial and/or stromal cells), instead of individual cells, entering the lymphatic system. However, from the endothelium's perspective, we should not underestimate the reactivity and plasticity of lymphatic vessels in the process. The lymphangiogenesis (Fig. 4h), endothelial invagination (Fig. 4f, g), vasodilation (Fig. 6), and abnormal lymphatic network integration between the pancreas and intestine (Fig. 4d) also suggest an active role – rather than a passive target – of the lymphatic vessels in the metastasis of pancreatic cancer.

Although the definition of lymphangiogenesis refers to the formation of lymphatic vessels (or walls), in Fig. 5 we detect the formation of lymphatic luminal tubules in lymphangiogenesis, which extend across the luminal space in a neoplastic microenvironment. In the normal pancreas, the Lyve1$^+$ bridges are only seen in the subcapsular sinus of the lymph node (Fig. 2c, d), but they appear outside the lymph node in large-scale duct lesion formation (Fig. 5a–e). Morphologically, the small, elongated tubule (Fig. 5c and Supplementary Video S3) cannot be easily detected with the standard microtome-based histology (3–5 μm in slide thickness), which explains why the structure has not been previously reported in the lesion microenvironment. Regarding the potential functions of the tubules, we speculate that they may: (i) form the lymphatic valves, (ii) create passages for lymphocyte migration (e.g., from the lymph node to the surrounding pancreatic lobules) (Supplementary Video S3), (iii) serve as the framework to mechanically support the thin-walled lymphatic vessel in tissue remodeling, and (iv) increase the overall endothelial cell density to prepare for further expansion of the network.

The apparent limitation of the D2-40/Lyve1immunodetection of the lymphatic network is that we cannot determine if the lymphatic vessels are indeed functional. The functional test, however, requires in vivo lymphatic imaging [40,41], which is not compatible with the tissue-clearing condition due to the unphysiological environment, such as the high osmotic pressure, created by the clearing reagent [42]. Without tissue clearing, deep-tissue optical microscopy is limited by light scattering in signal detection and thus cannot resolve the tissue structure and network in space. Despite the limitation in in vivo application, the technical advances in high-definition 3-D lymphatic network imaging and its integration with H&E histology (Fig. 1c; the gold standard in pathology) and neural imaging (Fig. 1b and 6) underline the resolving power and versatility of this approach in investigating the pancreatic tissue networks in the clinical and experimental conditions [25,43–46]. Finally, from the perspective of cancer model development, although neither the transgenic nor the orthotopic models can fully recapitulate the PanIN and PDAC progression in the human pancreas [47–49], our 3-D detection of the peri-lesional lymphangiogenesis in both conditions reflects the generic response of the lymphatic system in immune surveillance against the transformed cells in the experimental conditions.

In summary, using the human and mouse pancreases, we characterized the pancreatic lymphatic network in health and cancer progression. Prior to this study, the PanIN-lymphatic network association has not been systematically studied due to the lack of 3-D image data to present the lesion and the lymphatic network in a global and integrated fashion. Here, the high-definition 3-D images and videos provide novel insights into the peri-lesional lymphatic endothelial remodeling. Our work will build the technical and morphological foundation for future systematic detection and 3-D analysis of lymphatic vessel invasion in the cancer microenvironment.

Supplementary data to this article can be found online at https://doi.org/10.1016/j.ebiom.2019.08.044.

Acknowledgments

The authors are grateful for the support from the confocal imaging core in National Tsing Hua University, which is sponsored by the Ministry of Science and Technology, Taiwan (MOST 104-2731-M-007-002). We thank Chien-Chang Su for his work on assisting the establishment of Pan18 cell line.

Author contributions

All authors contributed to the study concept and design; C.N.S. and C.C.H. established the genetically engineered mouse models of pancreatic cancer; C.N.S., C.R.H., and K.S.G. generated the Pan18 cell line and syngeneic pancreatic tumor mouse model; T.C.C., C.Y.L., Y.M.J., and Y.W.T. contributed to human specimen acquisition and preparation; S.J.P., H.J.C., M.H.C., Y.H.C., and S.C.T. contributed to 3-D histology; C.N.S., K.S.G., Y.W.T., S.K., P.J.P., and S.C.T. contributed to 3-D image presentation; C.N.S., Y.W.T., and S.C.T. contributed to drafting of the manuscript. C.N.S., Y.W.T., and S.C.T. obtained funding. All authors contributed to data analysis and interpretation of data, revised the manuscript critically for intellectual content, and approved the final version of the manuscript.

Grant support

This work was supported in part by grants from Taiwan Academia Sinica (AS-107-TP-L15 & AS-105-TP-B15) and Ministry of Science and Technology (MOST 106-2321-B-001-048 & 106-0210-01-15-02) to C.N.S., MOST (106-2321-B-002-034) to Y.W.T., and Taiwan National Health Research Institutes (NHRI- EX107-10524EI) and MOST (106-2314-B-007-004-MY2) to S.C.T.

Disclosure of competing interest

The authors in this manuscript have no conflicts of interest to disclose.

References

[1] O'Morchoe CC. Lymphatic system of the pancreas. Microsc Res Tech 1997;37(5–6):456–77.
[2] Cesmebasi A, Malefant J, Patel SD, Du Plessis M, Renna S, Tubbs RS, et al. The surgical anatomy of the lymphatic system of the pancreas. Clin Anat 2015;28(4):527–37.
[3] DiMagno EP, Reber HA, Tempero MA. AGA technical review on the epidemiology, diagnosis, and treatment of pancreatic ductal adenocarcinoma. American Gastroenterological Association. Gastroenterology 1999;117(6):1464–84.
[4] Pawlik TM, Gleisner AL, Cameron JL, Winter JM, Assumpcao L, Lillemoe KD, et al. Prognostic relevance of lymph node ratio following pancreaticoduodenectomy for pancreatic cancer. Surgery 2007;141(5):610–8.
[5] Slidell MB, Chang DC, Cameron JL, Wolfgang C, Herman JM, Schulick RD, et al. Impact of total lymph node count and lymph node ratio on staging and survival after pancreatectomy for pancreatic adenocarcinoma: a large, population-based analysis. Ann Surg Oncol 2008;15(1):165–74.
[6] Riediger H, Keck T, Wellner U, zur Hausen A, Adam U, Hopt UT, et al. The lymph node ratio is the strongest prognostic factor after resection of pancreatic cancer. J Gastrointest Surg 2009;13(7):1337–44.
[7] Fink DM, Steele MM, Hollingsworth MA. The lymphatic system and pancreatic cancer. Cancer Lett 2016;381(1):217–36.
[8] Hruban RH, Adsay NV, Albores-Saavedra J, Compton C, Garrett ES, Goodman SN, et al. Pancreatic intraepithelial neoplasia: a new nomenclature and classification system for pancreatic duct lesions. Am J Surg Pathol 2001;25(5):579–86.
[9] di Magliano MP, Logsdon CD. Roles for KRAS in pancreatic tumor development and progression. Gastroenterology 2013;144(6):1220–9.
[10] Guerra C, Schuhmacher AJ, Canamero M, Grippo PJ, Verdaguer L, Perez-Gallego L, et al. Chronic pancreatitis is essential for induction of pancreatic ductal adenocarcinoma by K-Ras oncogenes in adult mice. Cancer Cell 2007;11(3):291–302.
[11] Lowenfels AB, Maisonneuve P, Cavallini G, Ammann RW, Lankisch PG, Andersen JR, et al. Pancreatitis and the risk of pancreatic cancer. International Pancreatitis Study Group. N Engl J Med 1993;328(20):1433–7.
[12] Houbracken I, de Waele E, Lardon J, Ling Z, Heimberg H, Rooman I, et al. Lineage tracing evidence for transdifferentiation of acinar to duct cells and plasticity of human pancreas. Gastroenterology 2011;141(2):731–41 41 e1-4.
[13] Habbe N, Shi G, Meguid RA, Fendrich V, Esni F, Chen H, et al. Spontaneous induction of murine pancreatic intraepithelial neoplasia (mPanIN) by acinar cell targeting of oncogenic Kras in adult mice. Proc Natl Acad Sci U S A 2008;105(48):18913–8.
[14] Omary MB, Lugea A, Lowe AW, Pandol SJ. The pancreatic stellate cell: a star on the rise in pancreatic diseases. J Clin Invest 2007;117(1):50–9.
[15] Apte MV, Wilson JS, Lugea A, Pandol SJ. A starring role for stellate cells in the pancreatic cancer microenvironment. Gastroenterology 2013;144(6):1210–9.
[16] Neesse A, Algul H, Tuveson DA, Gress TM. Stromal biology and therapy in pancreatic cancer: a changing paradigm. Gut 2015;64(9):1476–84.
[17] Demir IE, Friess H, Ceyhan GO. Nerve-cancer interactions in the stromal biology of pancreatic cancer. Front Physiol 2012;3:97.
[18] Lin PY, Peng SJ, Shen CN, Pasricha PJ, Tang SC. PanIN-associated pericyte, glial, and islet remodeling in mice revealed by 3D pancreatic duct lesion histology. Am J Physiol Gastrointest Liver Physiol 2016;311(3):G412–22.
[19] Kurahara H, Takao S, Maemura K, Shinchi H, Natsugoe S, Aikou T. Impact of vascular endothelial growth factor-C and -D expression in human pancreatic cancer: its relationship to lymph node metastasis. Clin Cancer Res 2004;10(24):8413–20.
[20] Kitadai Y, Kodama M, Cho S, Kuroda T, Ochiumi T, Kimura S, et al. Quantitative analysis of lymphangiogenic markers for predicting metastasis of human gastric carcinoma to lymph nodes. Int J Cancer 2005;115(3):388–92.
[21] White JD, Hewett PW, Kosuge D, McCulloch T, Enholm BC, Carmichael J, et al. Vascular endothelial growth factor-D expression is an independent prognostic marker for survival in colorectal carcinoma. Cancer Res 2002;62(6):1669–75.
[22] Stacker SA, Achen MG, Jussila L, Baldwin ME, Alitalo K. Lymphangiogenesis and cancer metastasis. Nat Rev Cancer 2002;2(8):573–83.
[23] Saharinen P, Tammela T, Karkkainen MJ, Alitalo K. Lymphatic vasculature: development, molecular regulation and role in tumor metastasis and inflammation. Trends Immunol 2004;25(7):387–95.
[24] Tang SC, Shen CN, Lin PY, Peng SJ, Chien HJ, Chou YH, et al. Pancreatic neuro-insular network in young mice revealed by 3D panoramic histology. Diabetologia 2018;61(1):158–67.
[25] Tang SC, Baeyens L, Shen CN, Peng SJ, Chien HJ, Scheel DW, et al. Human pancreatic neuro-insular network in health and fatty infiltration. Diabetologia 2018;61(1):168–81.
[26] Chien HJ, Peng SJ, Hua TE, Kuo CH, Juang JH, Tang SC. 3-D imaging of islets in obesity: formation of the islet-duct complex and neurovascular remodeling in young hyperphagic mice. Int J Obes (Lond) 2016;40(4):685–97.
[27] Kahn HJ, Bailey D, Marks A. Monoclonal antibody D2-40, a new marker of lymphatic endothelium, reacts with Kaposi's sarcoma and a subset of angiosarcomas. Mod Pathol 2002;15(4):434–40.
[28] Liu YA, Chung YC, Pan ST, Shen MY, Hou YC, Peng SJ, et al. 3-D imaging, illustration, and quantitation of enteric glial network in transparent human colon mucosa. Neurogastroenterol Motil 2013;25(5):e324–38.
[29] Neradil J, Veselska R. Nestin as a marker of cancer stem cells. Cancer Sci 2015;106(7):803–11.
[30] Juang JH, Peng SJ, Kuo CH, Tang SC. Three-dimensional islet graft histology: panoramic imaging of neural plasticity in sympathetic reinnervation of transplanted islets under the kidney capsule. Am J Physiol Endocrinol Metab 2014;306(5):E559–70.
[31] Banerji S, Ni J, Wang SX, Clasper S, Su J, Tammi R, et al. LYVE-1, a new homologue of the CD44 glycoprotein, is a lymph-specific receptor for hyaluronan. J Cell Biol 1999;144(4):789–801.
[32] Prevo R, Banerji S, Ferguson DJ, Clasper S, Jackson DG. Mouse LYVE-1 is an endocytic receptor for hyaluronan in lymphatic endothelium. J Biol Chem 2001;276(22):19420–30.
[33] Tripp CH, Haid B, Flacher V, Sixt M, Peter H, Farkas J, et al. The lymph vessel network in mouse skin visualised with antibodies against the hyaluronan receptor LYVE-1. Immunobiology 2008;213(9–10):715–28.
[34] Xu H, Chen M, Reid DM, Forrester JV. LYVE-1-positive macrophages are present in normal murine eyes. Invest Ophthalmol Vis Sci 2007;48(5):2162–71.
[35] Attout T, Hoerauf A, Denece G, Debrah AY, Marfo-Debrekyei Y, Boussinesq M, et al. Lymphatic vascularisation and involvement of Lyve-1+ macrophages in the human onchocerca nodule. PLoS One 2009;4(12):e8234.
[36] Braun A, Worbs T, Moschovakis GL, Halle S, Hoffmann K, Bolter J, et al. Afferent lymph-derived T cells and DCs use different chemokine receptor CCR7-dependent routes for entry into the lymph node and intranodal migration. Nat Immunol 2011;12(9):879–87.
[37] Almoguera C, Shibata D, Forrester K, Martin J, Arnheim N, Perucho M. Most human carcinomas of the exocrine pancreas contain mutant c-K-ras genes. Cell 1988;53(4):549–54.

[38] Hingorani SR, Wang L, Multani AS, Combs C, Deramaudt TB, Hruban RH, et al. Trp53R172H and KrasG12D cooperate to promote chromosomal instability and widely metastatic pancreatic ductal adenocarcinoma in mice. Cancer Cell 2005;7(5):469–83.
[39] O'Connor TM, O'Connell J, O'Brien DI, Goode T, Bredin CP, Shanahan F. The role of substance P in inflammatory disease. J Cell Physiol 2004;201(2):167–80.
[40] Nune SK, Gunda P, Majeti BK, Thallapally PK, Forrest ML. Advances in lymphatic imaging and drug delivery. Adv Drug Deliv Rev 2011;63(10−11):876–85.
[41] Sevick-Muraca EM, Kwon S, Rasmussen JC. Emerging lymphatic imaging technologies for mouse and man. J Clin Invest 2014;124(3):905–14.
[42] Tainaka K, Kuno A, Kubota SI, Murakami T, Ueda HR. Chemical principles in tissue clearing and staining protocols for whole-body cell profiling. Annu Rev Cell Dev Biol 2016;32:713–41.
[43] Tang SC, Peng SJ, Chien HJ. Imaging of the islet neural network. Diabetes Obes Metab 2014;16(Suppl. 1):77–86.
[44] Juang JH, Kuo CH, Peng SJ, Tang SC. 3-D imaging reveals participation of donor islet Schwann cells and Pericytes in islet transplantation and graft neurovascular regeneration. EBioMedicine 2015;2(2):109–19.
[45] Tang SC, Jessup CF, Campbell-Thompson M. The role of accessory cells in islet homeostasis. Curr Diab Rep 2018;18(11):117.
[46] Chien HJ, Chiang TC, Peng SJ, Jeng YM, Tien YW, Tang SC. 3-D microscopy of human pancreatic intraepithelial neoplasia. Gastroenterology 2018;154(6):S516–7 Suppl 1.
[47] Eklund L, Bry M, Alitalo K. Mouse models for studying angiogenesis and lymphangiogenesis in cancer. Mol Oncol 2013;7(2):259–82.
[48] Mazur PK, Siveke JT. Genetically engineered mouse models of pancreatic cancer: unravelling tumour biology and progressing translational oncology. Gut 2012;61(10):1488–500.
[49] Herreros-Villanueva M, Hijona E, Cosme A, Bujanda L. Mouse models of pancreatic cancer. World J Gastroenterol 2012;18(12):1286–94.